Efficient organic solar cells with small energy losses based on a wide-bandgap trialkylsilyl-substituted donor polymer and a non-fullerene acceptor

Efficient organic solar cells with small energy losses based on a wide-bandgap trialkylsilyl-substituted donor polymer and a non-fullerene acceptor

Haijun Bin [a], Tom P.A. van der Pol [a], Junyu Li [a], Bas T. van Gorkom [a], Martijn M. Wienk [a], René A.J. Janssen [a,b,*]

[a] Molecular Materials and Nanosystems & Institute for Complex Molecular Systems, Eindhoven University of Technology, P.O. Box 513, 5600 MB Eindhoven, The Netherlands

[b] Dutch Institute for Fundamental Energy Research, De Zaale 20 5612 AJ, Eindhoven, The Netherlands

ABSTRACT

Efficient organic solar cells based on a blend of PBDS-T as a donor polymer and BTP-eC9 as non-fullerene acceptor are presented and characterized. PBDS-T is an alternating copolymer that comprises easily accessible electron-rich trialkylsilyl-substituted benzodithiophene and electron-deficient benzodithiophene-4,8-dione units and that can be efficiently and reproducibly synthesized in high molecular weights, while keeping good solubility. PBDS-T exhibits a strong absorption between 450 and 700 nm and combines a wide optical bandgap of 1.86 eV, with low-lying energy levels, and a face-on molecular orientation in thin films. Organic solar cells prepared by blending PBDS-T with BTP-eC9 show considerable performance when as-cast films are annealed in solvent vapor and present a high open-circuit voltage of 0.86 V, a low photon-energy loss of 0.53 eV, and an internal quantum efficiency of 93%. The power conversion efficiency reaches 16.4%, which − to the best of our knowledge − is the highest for a conjugated polymer comprising trialkylsilyl side chains in combination with a Y6-based non-fullerene acceptor. Specifically, the trialkylsilyl side-chains of PBDS-T reduce synthetic complexity, result in a low energy loss by ensuring low energetic disorder, and provide competitive device performance.

1. Introduction

Organic solar cells (OSCs) continue to attract significant interest for photovoltaic energy conversion because they combine intrinsic advantages, including potential low cost and large area manufacturing, lightweight, semi-transparency, and flexibility with a high power conversion efficiency (PCE) [1–3]. The revolutionary progress in the design and synthesis of innovative non-fullerene acceptors (NFAs) such as ITIC, Y6 (Fig. 1), and their derivatives in recent years [4–8], has resulted in the optimization of the long-wavelength absorption and electronic properties that provide enhanced photocurrent density, reduced voltage loss, and significantly improved the PCE to 17–19% [9–20]. Next to the acceptor, selecting a suitable donor polymer remains critical for achieving efficient OSCs. Currently, the most popular polymer donor is PM6 (Fig. 1), an alternating copolymer composed of electron-donating fluorinated benzodithiophene (FBDT) units and electron-deficient

benzodithiophene-4,8-dione (BDD) units that is wildly employed as donor in bulk-heterojunction blends with state-of-the-art acceptors to obtain highly efficient devices [5,9,10,21–27]. However, intrinsic shortcomings of PM6, including the fact that its performance is highly sensitive to the molecular weight and a cumbersome synthesis of its precursor intermediates, leads to considerable batch-to-batch variations in device performance and high materials costs, which may limit future commercialization and industrialization of OSCs [28–30]. Therefore, development of high-performing donor polymers with superior synthetic reproducibility at reduced cost deserves further attention.

One of the main reasons for the success of PM6 are the fluorine atoms in the conjugated side chains that effectively down-shift the molecular energy levels of PM6 while enhancing the intermolecular interaction. These features are beneficial for achieving a high open-circuit voltage (V_{oc}) and an improved charge carrier mobility that enhance the photovoltaic performance [31]. On the other hand, also drawbacks of

fluorination exist. These include the tedious synthesis and purification of fluorine-containing intermediates that contribute to a high synthetic complexity for PM6 [28,30]. Moreover, to suppress excessive molecular aggregation of PM6 in the active layer and optimize the bulk-heterojunction morphology, it is generally necessary to use halogen-containing high boiling point additives, such as 1,8-diiodooctane or 1-chloronaphthalene [9,11,15,32,33], in cell fabrication which may hamper device stability and complicate future high-throughput processing because of a largely increased drying time of the active layer. With the rapid development of OSCs, it is essential to design polymers that offer high efficiency, low cost, and easy processing.

Trialkylsilyl side chains have emerged as a valuable building block strategy in side-chain engineering for conjugated polymers, because they also efficiently down-shift molecular energy levels and improve crystallinity and hole mobility [34–37]. By adopting trialkylsilyl-substituted benzodithiophene units (BDTSi) in copolymers with benzotriazole (BTA) units, efficient donors such as J70, J71, and J101 have been constructed [34,35,37,38]. When blending these polymers with ITIC and their derivatives, the photovoltaic devices show high exciton dissociation and charge separation efficiencies, resulting in excellent device performance. In addition to these electronic characteristics, another important advantage of BDTSi is its convenient synthesis involving a short and high-yield synthetic procedure, which is a desirable feature towards commercialization [39]. Unfortunately, the J-series of polymers only exhibit competitive PCEs in ITIC-based OSCs. In the Y6-based OSCs, which currently represent the forefront of organic photovoltaics, polymer donors containing trialkylsilyl side chains have only very recently been shown to be useful. First, Wang et al. used a chlorinated BDTSi monomer to synthesize PBDS-TCl (Fig. 1) as a copolymer with BDD to blend it with the Y6-derived acceptor BTP-eC9 (Fig. 1) [40]. While binary PBDS-TCl:BTP-eC9 blends provided only moderate PCEs up to 5.4%, replacing 10% of PM6 in PM6:BTP-eC9 by PBDS-TCl resulted a PCE increase from 17.0% for the binary blend to 17.7% for the ternary system [40]. Second, Chen et al. used PBDS-TCl in combination with Y6 as acceptor to reach an efficiency of 14.6% [41]. The PBDS-TCl polymer provides a low energy loss of 0.41 eV as a result of a high V_{oc} of 0.92 V and a bandgap of 1.33 eV for the Y6 acceptor [41].

Herein, we use the non-chlorinated version, PBDS-T (Fig. 1) [42] and investigate its optical, electrical, and photovoltaic properties in combination with BTP-eC9 [15]. PBDS-T was previously blended with ITIC, affording a PCE of 11.1% [42]. We find that OSCs based on PBDS-T and BTP-eC9 provide PCEs of 16.4% when using a simple post-treatment by solvent vapor annealing (SVA). PBDS-T:BTP-eC9 solar cells demonstrate a low minimum photon-loss energy (E_{loss}) of 0.53 eV, and combine this with a high internal quantum efficiency of 93%. PBDS-T is thus a promising low-cost polymer donor for application in efficient OSCs.

2. Results and discussion

2.1. Synthesis and opto-electronic properties

PBDS-T was synthesized using BDTSi and BDD as monomers in a palladium-catalyzed Stille polymerization reaction with an extremely high yield of over 95%. The synthesis followed procedures described by Chen et al. [42] and is described in the Experimental Section in the Supporting Information. To check the synthetic reproducibility, five different batches of PBDS-T were synthesized. The number-average molecular weight (M_n) and polydispersity index (PDI) are in the range of $M_n = 60$–95 kDa with PDI = 2–3. Despite its relatively high M_n, PBDS-T shows good solubility in chlorobenzene (CB), which was therefore used to process the active layers for OSC fabrication. Differential scanning calorimetry (DSC) thermograms of PBDS-T (Fig. S1) did not show any clear endothermic or exothermic peaks associated with melting or crystallization between 20 and 350 °C. PBDS-T has high thermal stability up to 380 °C [42].

The normalized UV–vis–NIR absorption spectra of PBDS-T, BTP-eC9, and the blend film are shown in Fig. 2a. PBDS-T exhibits a maximum absorption at 610 nm with an onset at about 666 nm, corresponding to a wide optical bandgap (E_g) of 1.86 eV. The optical absorption coefficient of PBDS-T is 1.7×10^5 cm^{-1} in thin films and 55.5 L g^{-1} cm^{-1} in chlorobenzene solution. BTP-eC9 shows a maximum absorption peak at 835 nm with an onset at 928 nm, corresponding to a narrow E_g of 1.34 eV. The complementary absorption spectra of PBDS-T and BTP-eC9 give rise to a blend that covers a wide spectral range, from 410 to 920 nm, which is beneficial for achieving high J_{sc}. To understand the aggregation behavior of PBDS-T in solution, the temperature-dependent aggregation in CB solutions has been studied by measuring the UV–vis–NIR absorption spectra between 20 and 100 °C (Fig. 2b). At 20 °C, PBDS-T
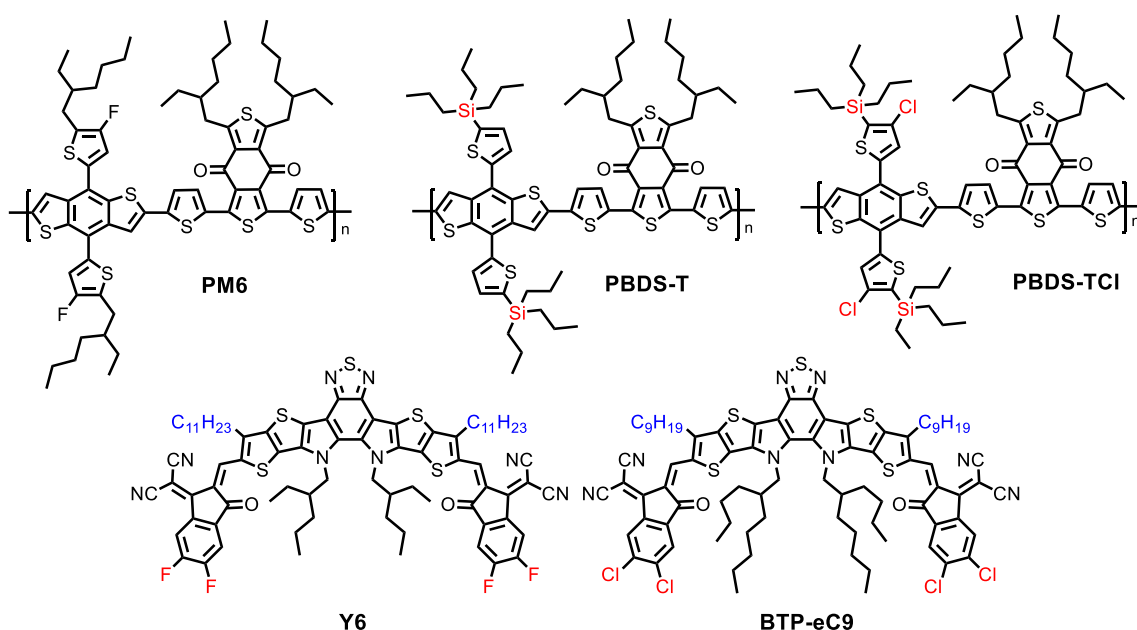

Fig. 1. Structures of polymer donors PM6, PBDS-T, and PBDS-TCl and of the non-fullerene acceptors Y6 and BTP-eC9 used in this work.
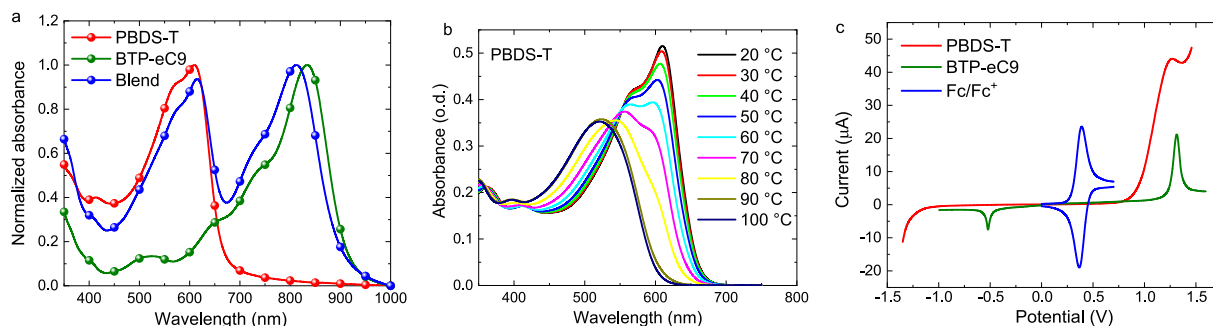
Fig. 2. (a) Normalized optical absorption spectra of PBDS-T, BTP-eC9, and their blend in thin films. (b) Optical absorption of PBDS-T in chlorobenzene (9.4 mg L^{-1}) as function of temperature. (c) Square-wave voltammograms of PBDS-T and BTP-eC9 on a platinum wire in 0.1 mol L^{-1} Bu$_4$NPF$_6$ acetonitrile solutions, recorded at a scan rate of 20 mV s^{-1}. Potentials are vs. Ag/AgCl.

shows a clear peak corresponding to the 0–0 transition and an additional shoulder of a 0–1 transition. When the temperature is increased, the absorption maximum shifts to the blue and the 0–0 peak gradually decreases in intensity. For PBDS-T the 0–0 peak has almost disappeared at 80 °C. Balancing the solubility, aggregation, and π–π stacking is important for achieving an optimal blend morphology [29].

The energy levels of PBDS-T and BTP-eC9 were measured by square wave voltammetry (SWV) under an inert atmosphere (Fig. 2c). A donor/acceptor-coated platinum wire, silver wire, and silver/silver chloride (Ag/AgCl) electrode served as working electrode, counter electrode, and quasi-reference electrode, respectively. The highest occupied molecular orbital (HOMO) and lowest unoccupied molecular orbital (LUMO) were determined from the onset potentials of the redox waves (E_{ox} and E_{red}) vs. a Ag/AgCl reference electrode. Absolute energies vs. vacuum were obtained using ferrocene/ferrocenium as internal standard ($E_{1/2}$(Fc/Fc$^+$) = 0.37 eV vs. Ag/AgCl) and using a value of -4.8 eV vs. vacuum for Fc/Fc$^+$, via $E_{HOMO/LUMO} = -q(E_{ox/red} - E_{1/2}(Fc/Fc^+) + 4.8)$ (eV). The HOMO and LUMO energy levels for PBDS-T and BTP-eC9 (Table 1) are well-matched with an offset that ensures efficient charge separation after photoexcitation. The rather deep HOMO energy level of PBDS-T originates from the trialkylsilyl side chains, which stabilize the HOMO and LUMO energy levels by the interaction between the low-lying σ* orbital of the Si atom and the π* orbital of the aromatic unit [34,43], and is expected to give higher V_{oc} and lower E_{loss} in OSCs.

2.2. Photovoltaic properties

Solar cells with a conventional device architecture (ITO/PEDOT:PSS/active layer/PFNBr/Ag) (ITO is indium tin oxide, PEDOT:PSS is poly(3,4-ethylenedioxythiophene) polystyrene sulfonate, and PFNBr is poly(9,9-bis(3′-(N,N-dimethyl)-N-ethylammoinium-propyl-2,7-fluorene)-*alt*-2,7-(9,9-dioctylfluorene))dibromide) were fabricated to investigate the photovoltaic properties of PBDS-T in OSCs. Optimized device performance was found using a donor:acceptor weight ratio of 1:1 and spin coating the mixture at a total concentration of 16 mg mL^{-1} in CB at 3000 rpm for 30 s, followed SVA by CS$_2$. The details of the device optimization procedures are shown in Fig. S2, Fig. S3, Table S1, and Table S2. Fig. 3a shows the current density–voltage (J-V) characteristics of optimized OSCs for as-cast and SVA blends. The corresponding photovoltaic parameters are summarized in Table 2. The as-cast PBDS-T:BTP-eC9 device displayed a PCE of 14.6%, with a high

$V_{oc} = 0.87$ V, $J_{sc} = 23.6$ mA cm^{-2}, and FF = 0.71 (FF is fill factor). Upon SVA of the active layer, the PCE of PBDS-T:BTP-eC9 based solar cells increased significantly to 15.5%, with a slightly reduced V_{oc} of 0.86 V, a higher J_{sc} of 24.4 mA cm^{-2}, and a higher FF of 0.74. Clearly, the SVA treatment for the PBDS-T-based film improved J_{sc} and FF, with a minimal loss in V_{oc} and thus delivered an improved PCE. The lower J_{sc} and FF of the as-cast active layers can be attributed to the inferior phase separation in this suboptimal as-cast morphology, as will be detailed below.

External quantum efficiency (EQE) spectra of the as-cast and SVA OSCs (Fig. 3b) demonstrate that both blends exhibit a high photoresponse in the 300–900 nm wavelength range, indicating efficient exciton separation and charge transport and collection. The high EQEs indicate that the mixing of PBDS-T with BTP-eC9 in the blend is intimate and that charge generation is not limited by a too coarse phase separation. The J_{sc} values integrated from the EQE spectra with the air mass 1.5 (AM1.5G) spectrum are 23.8 and 24.8 mA cm^{-2} for the as-cast and SVA devices, respectively and match within a few percent to the values obtained from the solar simulator, resulting from a slight mismatch between the solar simulator spectrum and the AM1.5G spectrum. The PCEs of the corresponding OSCs are 14.7% and 15.8% (Table 2). To test the batch-to-batch reproducibility, five different batches of PBDS-T were synthesized and blended with BTP-eC9. The five batches of PBDS-T have M_n's in the range of 60 to 95 kDa and provide PCEs close to 15% (Fig. S4 and Table S3), indicating that the performance is not very sensitive to the molecular weight. In addition, two other Y6 derivatives, Y6-BO-4Cl and Y6-BO-4F (Fig. S5), have been blended with PBDS-T and both devices also exhibit PCEs close to 15% (Fig. S6 and Table S4), implying that PBDS-T has good universality with state-of-the-art acceptors. For comparison, we summarize the photovoltaic data reported for OSCs based on non-fullerene acceptors and polymers comprising trialkylsilyl sidechains in Table S5. The table shows that the PCEs obtained here for PBDS-T and Y6 derivatives are generally higher than reported to date.

2.3. Studies on energy loss and charge recombination

The minimal photon-loss energy E_{loss}, which is the difference between the bandgap edge (E_g) and qV_{oc} (where q is the elementary charge) is a key factor limiting the photovoltaic performance. Reducing E_{loss} is imperative in further improving OSCs [44–49]. Following earlier work [14,44,47,50], we split E_{loss} into three contributions ($E_{loss} = \Delta E_1 + \Delta E_2 + \Delta E_3$): (1) the first is the unavoidable radiative recombination originating from absorption above the bandgap ($\Delta E_1 = E_g - qV_{oc}^{SQ}$), where qV_{oc}^{SQ} is known as the Shockley–Queisser (SQ) limit; (2) the second is due to additional radiative recombination from absorption below the bandgap, e.g. due to low-lying charge transfer states or strong disorder at the band edge ($\Delta E_2 = qV_{oc}^{SQ} - qV_{oc}^{rad\ below\ gap}$); (3) the third is the non-radiative recombination loss given by $\Delta E_3 = -(kT/q)ln(EQE_{EL})$, where EQE_{EL} is electroluminescence (EL) quantum efficiency of the solar cell, k the Boltzmann constant, and T the absolute temperature. In order to

Table 1
Physicochemical properties of PBDS-T and BTP-eC9.

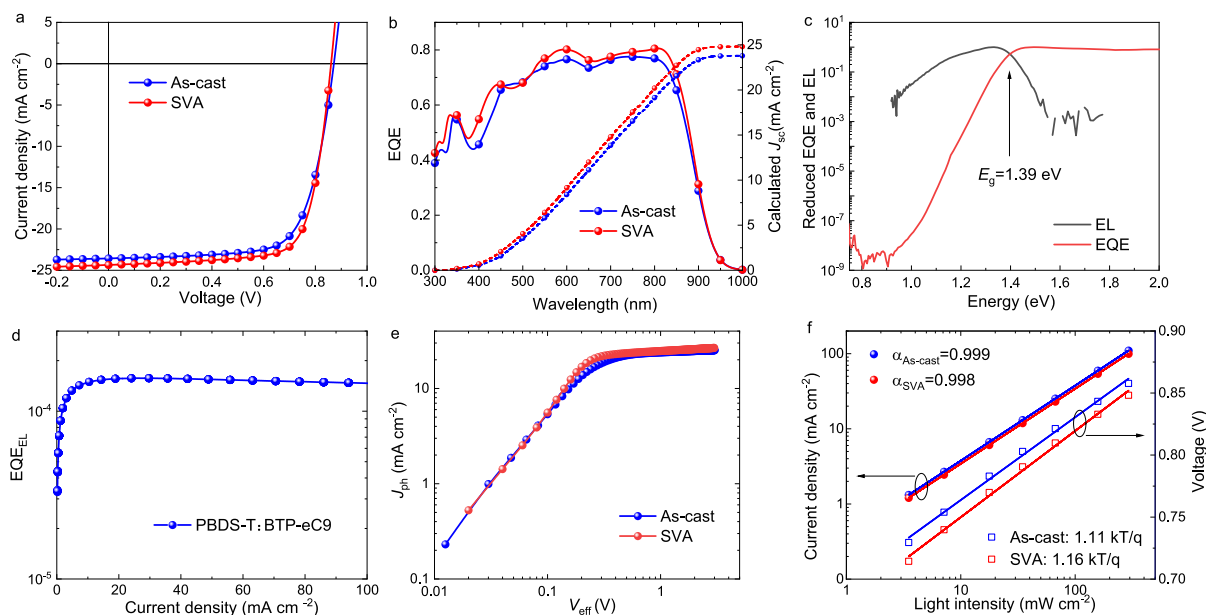| Material	λ_{onset} (nm)	E_g (eV)	E_{ox}(V)	E_{HOMO} (eV)	E_{red} (V)	E_{LUMO} (eV)
PBDS-T	666	1.86	0.95	-5.38	-1.26	-3.17
BTP-eC9	928	1.34	1.23	-5.66	-0.42	-4.01

Fig. 3. (a) J–V characteristics of the as-cast and SVA OSCs based on PBDS-T:BTP-eC9. (b) EQE spectra of the corresponding devices. (c) Reduced EQE and EL spectra of the PBDS-T:BTP-eC9 based device. (d) EQE_{EL} of the optimized device. (e) J_{ph} versus V_{eff} curves of as-cast and SVA devices. (f) Light intensity dependence of J_{sc} and V_{oc}.

Table 2
Photovoltaic parameters of OSCs measured with simulated AM1.5G (100 mW cm^{-2}) illumination.

Devices	MgF$_2$	J_{sc}[a](mA cm^{-2})	V_{oc}(V)	FF	PCE[a](%)	J_{sc}[b](mA cm^{-2})	PCE[b](%)
As-cast	no	23.6(23.16 ± 0.297)	0.87(0.86 ± 0.007)	0.71(0.69 ± 0.011)	14.6 (13.81 ± 0.370)	23.8	14.7
SVA	no	24.4(24.13 ± 0.167)	0.86(0.86 ± 0.004)	0.74(0.72 ± 0.012)	15.5(15.0 ± 0.326)	24.8	15.8
SVA	yes	25.5(25.14 ± 0.159)	0.86(0.86 ± 0.004)	0.74(0.73 ± 0.007)	16.2(15.81 ± 0.217)	25.8	16.4

[a] Values from J–V measurement. [b] Values from EQE measurement. The data outside the brackets is the highest value, and the data inside the brackets is the average value calculated from 8 individual solar cells.

understand E_{loss} of optimized PBDS-T:BTP-eC9 based OSCs, we measured the EQE in the sub-bandgap region and the EL spectrum. We determine the bandgap as $E_g = 1.393$ eV where the normalized reduced EQE and EL spectra intersect (Fig. 3c) [48]. An alternative method to determine the bandgap, by taking the photon energy where the first derivative of the EQE spectrum maximizes, gives the same value of $E_g = 1.393$ eV. To determine the non-radiative loss we measured the EQE_{EL} (Fig. 3d). Following reported work [14], the loss values obtained are $\Delta E_1 = 0.270$ eV, $\Delta E_2 = 0.035$ eV, and $\Delta E_3 = 0.226$ eV, resulting in an overall E_{loss} of 0.531 eV. Together with $E_g = 1.393$ eV, $E_{loss} = 0.531$ eV reproduces the experimental qV_{oc} of 0.86 eV accurately, showing the consistency of the analysis. $E_{loss} = 0.53$ eV is slightly less than the reported PM6:BTP-eC9 based OSCs ($E_{loss} = 0.561$ eV) [15], and similar to that of state-of-the-art non-fullerene-based devices [14,49]. Comparison with the loss contributions determined for PM6:BTP-eC9 ($\Delta E_1 = 0.263$ eV, $\Delta E_2 = 0.058$ eV, and $\Delta E_3 = 0.227$ eV) reveals that the difference is in ΔE_2, which is the voltage loss due to radiative recombination below the gap as a consequence of the non-abrupt, sloped absorption edge [15]. The relatively large non-radiative recombination loss ($\Delta E_3 = 0.226$ eV) leaves room for further optimization. Reducing this value is the main challenge for OSCs. Non-radiative recombination can occur at the interfaces with the charge transport layers and electrodes or at traps states in the bulk that could be caused by impurities, defects in the polymer chain or acceptor molecule, or morphology. It can also be caused by recombination of charges into low-lying triplet states of the donor or acceptor. Improvements must be found by reducing these loss processes.

The relatively small value for ΔE_2 is in accordance with the fact that the sub-bandgap EQE spectrum does not show the characteristic

absorption of a charge-transfer (CT) state, but rather an exponentially decaying band edge that can be fitted with an Urbach energy of $E_u \approx 20.8$ meV. The CT absorption is completely hidden under the local exciton absorption of BTP-eC9. The value is also less than $E_u = 24.1$ meV reported for PM6:BTP-eC9 [15], consistent with the lower value for ΔE_2. Kaiser et al. recently showed that for many pure and blended organic semiconductors the sub-bandgap absorption is dominated by thermal broadening and that the Urbach energy equals the thermal energy [51]. However, in the case of PBDS-T:BTP-eC9 the apparent Urbach energy $E_U^{app}(E) = [dln(EQE)/dE]^{-1}$ is ~ 20.8 meV and appreciably less than the thermal energy (25.4 meV at 295 K) in the sub-bandgap region between 1.05 and 1.30 eV as shown in Fig. S7a. The expression derived by Kaiser et al. for the absorption coefficient of a localized ground state and a significantly more diffuse delocalized excited state in a Gaussian density of states (DOS) does not give a good fit to the experimental data for energies below 1.3 eV (Fig. S7b). Irrespective of the nature of these differences in the apparent Urbach energy, its low value and the low standard deviation of the Gaussian DOS of $\sigma_s = 35$ meV found (Fig. S7b), indicate that there is little disorder at the band edge, which is beneficial for reaching a high V_{oc}.

To gain more insight into the effect of SVA on the photovoltaic performance, the exciton dissociation and charge collection properties of as-cast and SVA OSCs were investigated by measuring the dependence of the photocurrent density (J_{ph}) on the effective voltage (V_{eff}). The exciton dissociation efficiency (η_{diss}) and charge collection efficiency (η_{coll}) can be estimated from J_{ph} divided by J_{sat} (the saturated photocurrent density) under short circuit and maximum power output conditions. Fig. 3e shows that both η_{diss} and η_{coll} increase after SVA OSCs,

from 91.9% to 93.6% and from 86.4% to 88.5%, respectively. This indicates that SVA improves the exciton dissociation and charge collection efficiencies that are responsible for the high J_{sc} and FF, and the optimal device performance. The charge recombination in the two devices was studied by measuring the light intensity (P_{light}) dependence of J_{sc} and V_{oc}. The slopes of J_{sc} vs. P_{light} are very close to 1 in a double logarithmic plot for both (Fig. 3f), indicating negligible bimolecular recombination at short circuit. In a semi-logarithmic plot, the slope of V_{oc} vs. P_{light} is close to the thermal energy (kT/q) (Fig. 3f) and provided ideality factors of 1.11 (as cast) and 1.16 (after SVA). For trap-assisted Shockley-Read-Hall (SRH) recombination with equal capture coefficients for electrons and holes an ideality factor of 2 is expected. For pure bimolecular (band-to-band) recombination the expected ideality factor is 1. This suggests that trap-assisted recombination is not the major recombination pathway in PBDS-T:BTP-eC9 blends, both with and without SVA. We note, however, that also surface recombination due to non-selective contacts can reduce the ideality factor [52], such that the values close to 1 are not directly interpretable as being due to bimolecular recombination only.

2.4. Morphology studies

To further rationalize the high J_{sc} and FF for the SVA-based device, the morphologies of the as-cast and SVA films were studied in more detail. First, the surface morphologies of the pristine and blend films were investigated by atomic force microscopy (AFM) in tapping mode. Fig. S8 shows that the surface of the neat polymer film exhibits fiber-like textures with a small root-mean-squared surface roughness (R_q) of 0.40 nm, while the neat acceptor film exhibits cluster-like textures with R_q = 0.61 nm, implying a different surface organization for PBDS-T than for BTP-eC9. The higher R_q of BTP-eC9 suggests that its planar conjugated structure gives rise to stronger aggregation and crystallization. Fig. 4

shows the AFM height and phase images of the blend films with and without SVA. The two blend films have a similar R_q of 0.6 nm but show different surface features. After SVA, numerous well-distributed fibrous structures with a width of ~ 3 nm and length of ~ 8 nm can be seen in the phase image, suggesting a more ordered structure than that of the as-cast film. The higher order can enhance charge transport and increase J_{sc} and FF in the corresponding OSCs.

Second, the crystallinity of the films and nanostructure packing of PBDS-T, BTP-eC9, and their blends were investigated by two-dimensional grazing incidence wide-angle X-ray scattering (2D GIWAXS). The 2D GIWAXS diffraction patterns and line cut profiles are shown in Fig. 5. For the pure PBDS-T and BTP-eC9 films, the 2D GIWAXS patterns show stronger (010) diffraction signals in the out-of-plane (OoP) direction than in the in-plane (IP) direction. The (010) peaks for PBDS-T and BTP-eC9 are located at q_z ~ 1.63 and 1.72 Å^{-1} respectively, corresponding to π–π stacking distances (d_{010}) of 3.85 and 3.65 Å with crystallite coherence lengths (CCL$_{010}$) of 13.4 and 12.0 Å, respectively. For PBDS-T an IP diffraction peak at q_r = 0.29 Å^{-1} corresponds to a lamellar (100) spacing with d_{100} = 21.7 Å. The d-spacings and preferential face-on orientation of PBDS-T match to those reported previously, although the d_{010} spacing of 3.85 Å is slightly smaller than the value of 3.97 Å reported by Chen et al. [41]. BTP-eC9 shows a less defined IP diffraction signal at q_r = 0.43 Å^{-1}. Blending PBDS-T with BTP-eC9 does not change the stronger OoP compared to the IP (010) diffraction peaks. The as-cast blend film displays two (010) diffraction peaks in the OoP direction at q_z ~ 1.48 and 1.80 Å^{-1}. Apparently, there are two different types of π–π stacking in the blend film that do not correspond to those of either of the pure components. In the IP direction two diffraction peaks can be seen for the as-cast film at q_r = 0.28 and 0.44 Å^{-1}, positions that match with those of the pure components. After SVA, the two (010) peaks coalesce into a single diffraction peak at q_z = 1.70 Å^{-1}, i.e. in between q_z = 1.63 and 1.72 Å^{-1} of the pure compounds,
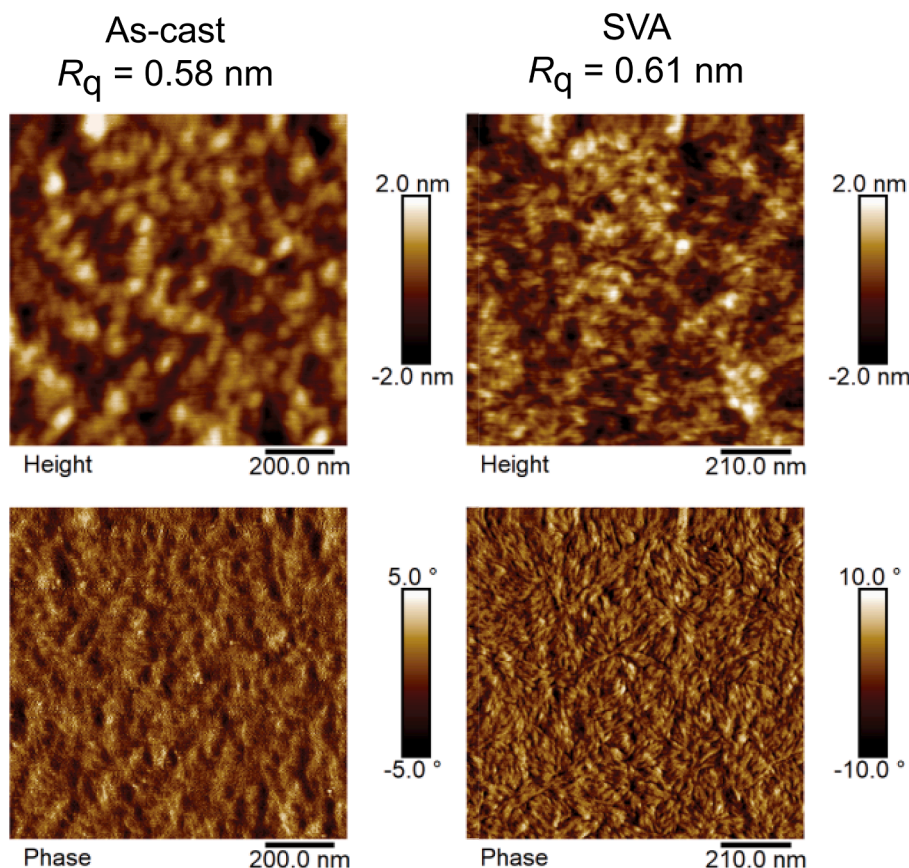

Fig. 4. AFM height and phase images of PBDS-T:BTP-eC9 blend films without or with SVA.
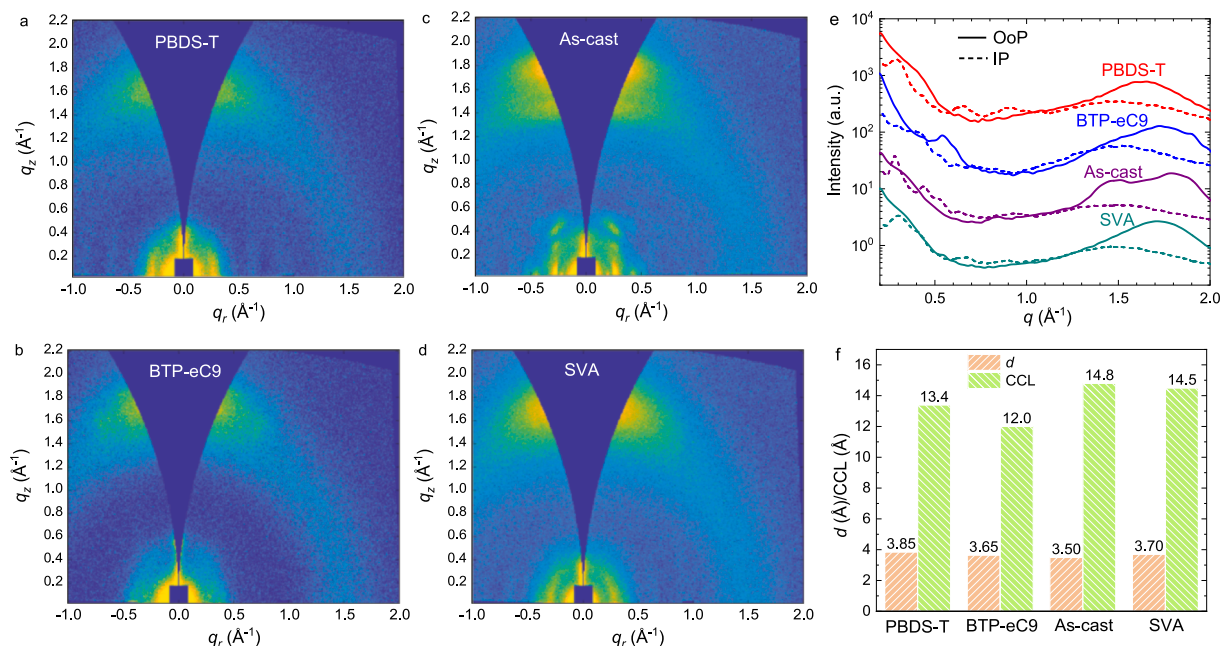
Fig. 5. (a-d) The 2D GIWAXS diffraction patterns of pristine (a, b) and blend films (c, d). (e) Corresponding line cut profiles. (f) d_{010} and CCL_{010} for pristine and blends films.

and corresponding to $d_{010} = 3.70$ Å and $CCL_{010} = 14.5$ Å. In the IP line cut of the SVA blend a peak at $q_r = 0.30$ Å^{-1} with a shoulder at $q_r = 0.44$ Å^{-1} indicate aggregates of the pure compounds. Together with the (010) peaks in the OoP direction, the distinct (100) peaks in the IP direction suggest that PBDS-T and BTP-eC9 have a preferred face-on orientation in the pure and blend films.

While AFM and 2D GIWAXS provide insight into the organization of

the PBDS-T:BTP-eC9 blend on a molecular level, future studies using e.g. grazing-incidence small-angle X-ray scattering (GISAXS) can address the dimensions of phase separation in more detail as has been shown for PM6:Y6 blends [5,53–55]. Nevertheless, high EQEs of up to 80% (Fig. 3b) already indicate that phase separation is not strongly limiting charge generation and collection. In fact, optical simulations presented in the next section show that the internal quantum efficiency (IQE) is
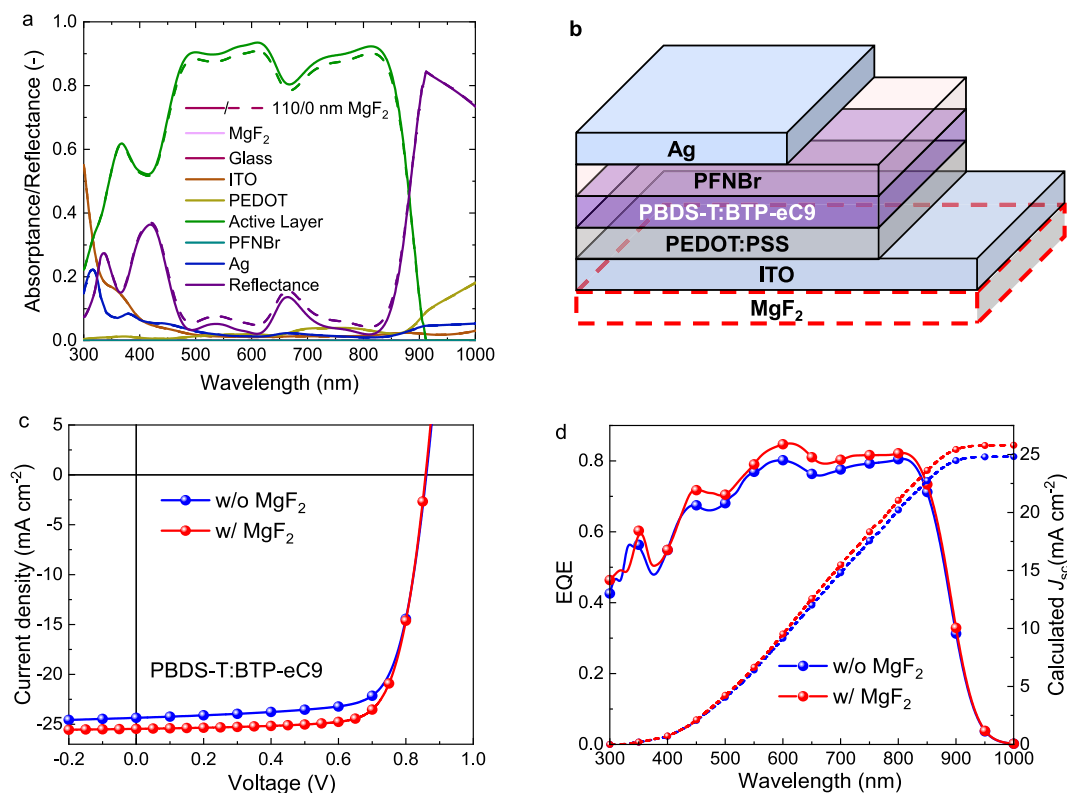

Fig. 6. (a) Reflectance and absorptance of individual layers from optical simulations for the entire device stack without/with 110 nm MgF$_2$. (b) The conventional device structure without/with MgF$_2$. (c) J–V characteristics of the PBDS-T-based OSCs without/with MgF$_2$. (d) EQE spectra of the corresponding devices.

above 90% when averaged over the AM1.5G spectrum.

2.5. Optical simulations

Next to the nature of the semiconductors and the morphology of the active layer, the optical properties of the device also affects the J_{sc}. Optical simulations using the transfer matrix method on the entire device stack help to understand the factors that limit J_{sc}. Fig. 6a reveals that next to the active layer, the ITO, PEDOT:PSS, and Ag layers absorb some of the incident light, but also that the main photon loss comes from the reflection of light. An effective strategy to reduce reflection is to introduce a MgF$_2$ layer on the side facing the light source because the refractive index of MgF$_2$ (~1.4) is smaller than that of glass (>1.5). [56,57] Because, reflection is proportional to the square of the difference in refractive indices at an interface, it will be reduced by making a graded transition from air to glass. The simulations indicate that a 110 nm MgF$_2$ layer reduces the reflection efficiently in the range of 450–850 nm, and increases the absorption of the active layer in the corresponding range, which helps to enhance the J_{sc}. Fig. S9 shows the optically simulated EQE spectra for a variety of MgF$_2$ film thicknesses. The simulations reveal that the optimal thickness is about 110 nm MgF$_2$ and would increase J_{sc} by approximately 1 mA cm^{-2}. We then fabricated a conventional OSC with the structure shown in Fig. 6b. Fig. 6c and 6d show the J-V curves and EQE spectra of the device without and with MgF$_2$ and the photovoltaic parameters are listed in Table 2. The experimental data shows good agreement with the optical simulations: with 110 nm MgF$_2$ the J_{sc} increased from 24.8 mA cm^{-2} to 25.8 mA cm^{-2}, and the PCE increased up to 16.4%. By integrating the experimental EQE and the simulated absorptance with the solar spectrum and taking their ratio, the AM1.5G spectral-averaged IQE is found to be 93%. The IQE spectra are shown in Fig S10.

3. Conclusions

In conclusion, we have shown that PBDS-T, an alternating copolymer based on electron-rich BDTSi units with trialkylsilyl side chains and electron-deficient BDD units, provides a wide optical bandgap, a deep HOMO energy level, and a preferential face-on molecular orientation. PBDS-T can be reproducibly synthesized in good yields and the absence of fluorine or chlorine substituents reduces its synthetic complexity. OSCs prepared by blending with the acceptor BTP-eC9 exhibited considerable performance, enhanced by solvent vapor annealing, with a small E_{loss} of 0.53 eV and high AM1.5G averaged internal quantum efficiency of 93%. With the help of a low refractive index antireflection layer, a PCE of 16.4% was achieved. PBDS-T is a first example of a polymer comprising trialkylsilyl side chains that can afford PCEs over 15% in combination with different Y6-based non-fullerene acceptors (BTP-eC9, Y6-BO-4Cl and Y6-BO-4F). The polymer can be synthesized in few steps with and gives good batch-to-batch reproducibility in OSCs. The study demonstrates that polymers containing trialkylsilyl side chains are a worthwhile option in combination with Y6-based non-fullerene derivatives provide efficient OSCs.

Declaration of Competing Interest

The authors declare that they have no known competing financial interests or personal relationships that could have appeared to influence the work reported in this paper.

Acknowledgements

Appendix A. Supplementary data

Supplementary data to this article can be found online at https://doi.org/10.1016/j.cej.2022.134878.

References

[1] Y. Li, Molecular design of photovoltaic materials for polymer solar cells: Toward suitable electronic energy levels and broad absorption, Acc. Chem. Res. 45 (2012) 723–733.

[2] L. Lu, T. Zheng, Q. Wu, A.M. Schneider, D. Zhao, L. Yu, Recent Advances in Bulk Heterojunction Polymer Solar Cells, Chem. Rev. 115 (23) (2015) 12666–12731.

[3] L. Ye, H. Hu, M. Ghasemi, T. Wang, B.A. Collins, J.-H. Kim, K. Jiang, J. H. Carpenter, H. Li, Z. Li, T. McAfee, J. Zhao, X. Chen, J.L.Y. Lai, T. Ma, J.-L. Bredas, H.e. Yan, H. Ade, Quantitative relations between interaction parameter, miscibility and function in organic solar cells, Nat. Mater. 17 (3) (2018) 253–260.

[4] Y. Lin, J. Wang, Z.-G. Zhang, H. Bai, Y. Li, D. Zhu, X. Zhan, An electron acceptor challenging fullerenes for efficient polymer solar cells, Adv. Mater. 27 (7) (2015) 1170–1174.

[5] J. Yuan, Y. Zhang, L. Zhou, G. Zhang, H.-L. Yip, T.-K. Lau, X. Lu, C. Zhu, H. Peng, P. A. Johnson, M. Leclerc, Y. Cao, J. Ulanski, Y. Li, Y. Zou, Single-Junction Organic Solar Cell with over 15% Efficiency Using Fused-Ring Acceptor with Electron-Deficient Core, Joule. 3 (4) (2019) 1140–1151.

[6] C. Yan, S. Barlow, Z. Wang, H. Yan, A.K.Y. Jen, S.R. Marder, X. Zhan, Non-fullerene acceptors for organic solar cells, Nat. Rev. Mater. 3 (2018) 1–19.

[7] J. Hou, O. Inganäs, R.H. Friend, F. Gao, Organic solar cells based on non-fullerene acceptors, Nat. Mater. 17 (2) (2018) 119–128.

[8] S. Li, C.-Z. Li, M. Shi, H. Chen, New Phase for Organic Solar Cell Research: Emergence of Y-Series Electron Acceptors and Their Perspectives, ACS Energy Lett. 5 (2020) 1554–1567.

[9] Y. Lin, B. Adilbekova, Y. Firdaus, E. Yengel, H. Faber, M. Sajjad, X. Zheng, E. Yarali, A. Seitkhan, O.M. Bakr, A. El-Labban, U. Schwingenschlögl, V. Tung, I. McCulloch, F. Laquai, T.D. Anthopoulos, 17% Efficient Organic Solar Cells Based on Liquid Exfoliated WS2 as a Replacement for PEDOT:PSS, Adv. Mater. 31 (46) (2019), 1902965, https://doi.org/10.1002/adma.201902965.

[10] L. Liu, Y. Kan, K. Gao, J. Wang, M. Zhao, H. Chen, C. Zhao, T. Jiu, A.K.Y. Jen, Y. Li, Graphdiyne Derivative as Multifunctional Solid Additive in Binary Organic Solar Cells with 17.3% Efficiency and High Reproductivity, Adv. Mater. 32 (11) (2020), 1907604, https://doi.org/10.1002/adma.201907604.

[11] L. Zhan, S. Li, T.-K. Lau, Y. Cui, X. Lu, M. Shi, C.-Z. Li, H. Li, J. Hou, H. Chen, Over 17% efficiency ternary organic solar cells enabled by two non-fullerene acceptors working in an alloy-like model, Energy Environ. Sci. 13 (2) (2020) 635–645.

[12] J. Yao, B. Qiu, Z.G. Zhang, L. Xue, R. Wang, C. Zhang, S. Chen, Q. Zhou, C. Sun, C. Yang, M. Xiao, L. Meng, Y. Li, Cathode engineering with perylene-diimide interlayer enabling over 17% efficiency single-junction organic solar cells, Nat. Commun. 11 (2020) 2726.

[13] R. Ma, T. Liu, Z. Luo, Q. Guo, Y. Xiao, Y. Chen, X. Li, S. Luo, X. Lu, M. Zhang, Y. Li, H.e. Yan, Improving open-circuit voltage by a chlorinated polymer donor endows binary organic solar cells efficiencies over 17%, Sci. China Chem. 63 (3) (2020) 325–330.

[14] P. Bi, S. Zhang, Z. Chen, Y.e. Xu, Y. Cui, T. Zhang, J. Ren, J. Qin, L. Hong, X. Hao, J. Hou, Reduced non-radiative charge recombination enables organic photovoltaic cell approaching 19% efficiency, Joule. 5 (9) (2021) 2408–2419.

[15] Y. Cui, H. Yao, J. Zhang, T. Zhang, Y. Wang, L. Hong, K. Xian, B. Xu, S. Yu, C. He, Z. Wei, F. Gao, J. Hou, Single-Junction Organic Photovoltaic Cells with Approaching 18% Efficiency, Adv. Mater. 1908205 (2020) 1908205.

[16] Q. Liu, Y. Jiang, K.e. Jin, J. Qin, J. Xu, W. Li, J.i. Xiong, J. Liu, Z. Xiao, K. Sun, S. Yang, X. Zhang, L. Ding, 18% efficiency organic solar cells, Sci. Bull. 65 (4) (2020) 272–275.

[17] S. Chen, L. Feng, T. Jia, J. Jing, Z. Hu, K. Zhang, F. Huang, High-performance polymer solar cells with efficiency over 18% enabled by asymmetric side chain engineering of non-fullerene acceptors, Sci. China Chem. 64 (7) (2021) 1192–1199.

[18] C. Li, J. Zhou, J. Song, J. Xu, H. Zhang, X. Zhang, J. Guo, L. Zhu, D. Wei, G. Han, J. Min, Y. Zhang, Z. Xie, Y. Yi, H.e. Yan, F. Gao, F. Liu, Y. Sun, Non-fullerene acceptors with branched side chains and improved molecular packing to exceed 18% efficiency in organic solar cells, Nat. Energy. 6 (6) (2021) 605–613.

[19] Y. Cui, Y. Xu, H. Yao, P. Bi, L. Hong, J. Zhang, Y. Zu, T. Zhang, J. Qin, J. Ren, Z. Chen, C. He, X. Hao, Z. Wei, J. Hou, Single-Junction Organic Photovoltaic Cell with 19% Efficiency, Adv. Mater. 33 (2021) 2102420.

[20] J. Wang, Z. Zheng, Y. Zu, Y. Wang, X. Liu, S. Zhang, M. Zhang, J. Hou, A Tandem Organic Photovoltaic Cell with 19.6% Efficiency Enabled by Light Distribution Control, Adv. Mater. 33 (2021) 2102787.

[21] Y. Cui, C. Yang, H. Yao, J. Zhu, Y. Wang, G. Jia, F. Gao, J. Hou, Efficient Semitransparent Organic Solar Cells with Tunable Color enabled by an Ultralow-Bandgap Nonfullerene Acceptor, Adv. Mater. 29 (2017) 1703080.

[22] C. Sun, S. Qin, R. Wang, S. Chen, F. Pan, B. Qiu, Z. Shang, L. Meng, C. Zhang, M. Xiao, C. Yang, Y. Li, High Efficiency Polymer Solar Cells with Efficient Hole Transfer at Zero Highest Occupied Molecular Orbital Offset between Methylated

Polymer Donor and Brominated Acceptor, J. Am. Chem. Soc. 142 (3) (2020) 1465–1474.

[23] Z. Luo, R. Ma, T. Liu, J. Yu, Y. Xiao, R. Sun, G. Xie, J. Yuan, Y. Chen, K. Chen, G. Chai, H. Sun, J. Min, J. Zhang, Y. Zou, C. Yang, X. Lu, F. Gao, H.e. Yan, Article Fine-Tuning Energy Levels via Asymmetric End Groups Enables Polymer Solar Cells with Efficiencies over 17 % Fine-Tuning Energy Levels via Asymmetric End Groups Enables Polymer, Joule. 4 (6) (2020) 1236–1247.

[24] G.P. Kini, S.J. Jeon, D.K. Moon, Design Principles and Synergistic Effects of Chlorination on a Conjugated Backbone for Efficient Organic Photovoltaics: A Critical Review, Adv. Mater. 32 (2020) 1906175.

[25] R. Sorrentino, E. Kozma, S. Luzzati, R. Po, Interlayers for non-fullerene based polymer solar cells: distinctive features and challenges, Energy Environ. Sci. 14 (1) (2021) 180–223.

[26] Z. Luo, T. Liu, R. Ma, Y. Xiao, L. Zhan, G. Zhang, H. Sun, F. Ni, G. Chai, J. Wang, C. Zhong, Y. Zou, X. Guo, X. Lu, H. Chen, H. Yan, C. Yang, Precisely Controlling the Position of Bromine on the End Group Enables Well-Regular Polymer Acceptors for All-Polymer Solar Cells with Efficiencies over 15%, Adv. Mater. 32 (2020) 2005942.

[27] Z. Luo, R. Ma, Z. Chen, Y. Xiao, G. Zhang, T. Liu, R. Sun, Q. Zhan, Y. Zou, C. Zhong, Y. Chen, H. Sun, G. Chai, K. Chen, X. Guo, J. Min, X. Lu, C. Yang, H. Yan, Altering the Positions of Chlorine and Bromine Substitution on the End Group Enables High-Performance Acceptor and Efficient Organic Solar Cells, Adv. Energy Mater. 10 (2020) 2002649.

[28] S. Pang, Z. Wang, X. Yuan, L. Pan, W. Deng, H. Tang, H. Wu, S. Chen, C. Duan, F. Huang, Y. Cao, A Facile Synthesized Polymer Featuring B-N Covalent Bond and Small Singlet-Triplet Gap for High-Performance Organic Solar Cells, Angew. Chem. - Int. Ed. 60 (16) (2021) 8813–8817.

[29] J. Wu, G. Li, J. Fang, X. Guo, L. Zhu, B. Guo, Y. Wang, G. Zhang, L. Arunagiri, F. Liu, H. Yan, M. Zhang, Y. Li, Random terpolymer based on thiophene-thiazolothiazole unit enabling efficient non-fullerene organic solar cells, Nat. Commun. 11 (2020) 4612.

[30] S. Zhang, Y. Qin, J. Zhu, J. Hou, Over 14% Efficiency in Polymer Solar Cells Enabled by a Chlorinated Polymer Donor, Adv. Mater. 30 (2018) 1800868.

[31] Q. Zhang, M.A. Kelly, N. Bauer, W. You, The Curious Case of Fluorination of Conjugated Polymers for Solar Cells, Acc. Chem. Res. 50 (9) (2017) 2401–2409.

[32] R. Yu, H. Yao, L. Hong, Y. Qin, J. Zhu, Y. Cui, S. Li, J. Hou, Design and application of volatilizable solid additives in non-fullerene organic solar cells, Nat. Commun. 9 (2018) 4645.

[33] Y. Cui, H. Yao, J. Zhang, T. Zhang, Y. Wang, L. Hong, K. Xian, B. Xu, S. Zhang, J. Peng, Z. Wei, F. Gao, J. Hou, Over 16% efficiency organic photovoltaic cells enabled by a chlorinated acceptor with increased open-circuit voltages, Nat. Commun. 10 (2019) 2515.

[34] H. Bin, L. Gao, Z.G. Zhang, Y. Yang, Y. Zhang, C. Zhang, S. Chen, L. Xue, C. Yang, M. Xiao, Y. Li, 11.4% Efficiency non-fullerene polymer solar cells with trialkylsilyl substituted 2D-conjugated polymer as donor, Nat. Commun. 7 (2016) 13651.

[35] H. Bin, L. Zhong, Y. Yang, L. Gao, H. Huang, C. Sun, X. Li, L. Xue, Z.G. Zhang, Z. Zhang, Y. Li, Medium Bandgap Polymer Donor Based on Bi(trialkylsilylthienyl-benzo[1,2-b:4,5-b″]-difuran) for High Performance Nonfullerene Polymer Solar Cells, Adv. Energy Mater. 7 (2017) 1700746.

[36] W. Su, G. Li, Q. Fan, Q. Zhu, X. Guo, J. Chen, J. Wu, W. Ma, M. Zhang, Y. Li, Nonhalogen solvent-processed polymer solar cells based on chlorine and trialkylsilyl substituted conjugated polymers achieve 12.8% efficiency, J. Mater. Chem. A. 7 (5) (2019) 2351–2359.

[37] H. Bin, Y. Yang, Z. Peng, L. Ye, J. Yao, L. Zhong, C. Sun, L. Gao, H. Huang, X. Li, B. Qiu, L. Xue, Z.G. Zhang, H. Ade, Y. Li, Effect of Alkylsilyl Side-Chain Structure on Photovoltaic Properties of Conjugated Polymer Donors, Adv. Energy Mater. 8 (2018) 1702324.

[38] H. Bin, I. Angunawela, R. Ma, A. Nallapaneni, C. Zhu, P.J. Leenaers, B.W.H. Saes, M.M. Wienk, H.e. Yan, H. Ade, R.A.J. Janssen, Effect of main and side chain chlorination on the photovoltaic properties of benzodithiophene-: Alt -benzotriazole polymers, J. Mater. Chem. C. 8 (43) (2020) 15426–15435.

[39] R. Xue, J. Zhang, Y. Li, Y. Li, Organic Solar Cell Materials toward Commercialization, Small. 14 (2018) 1801793.

[40] W. Peng, Y. Lin, S.Y. Jeong, Y. Firdaus, Z. Genene, A. Nikitaras, L. Tsetseris, H. Y. Woo, W. Zhu, T.D. Anthopoulos, E. Wang, Using Two Compatible Donor Polymers Boosts the Efficiency of Ternary Organic Solar Cells to 17.7%, Chem. Mater. 33 (18) (2021) 7254–7262.

[41] B. Huang, Y. Cheng, H. Jin, J. Liu, X. Huang, Y. Cui, X. Liao, C. Yang, Z. Ma, L. Chen, Alkylsilyl Fused Ring-Based Polymer Donor for Non-Fullerene Solar Cells with Record Open Circuit Voltage and Energy Loss, Small. 2104451 (2021), 210445.

[42] B. Huang, L. Chen, X. Jin, D. Chen, Y. An, Q. Xie, Y. Tan, H. Lei, Y. Chen, Alkylsilyl Functionalized Copolymer Donor for Annealing-Free High Performance Solar Cells with over 11% Efficiency: Crystallinity Induced Small Driving Force, Adv. Funct. Mater. 28 (2018) 1800606.

[43] J. Ohshita, Conjugated oligomers and polymers containing dithienosilole units, Macromol. Chem. Phys. 210 (17) (2009) 1360–1370.

[44] D. Veldman, S.C.J. Meskers, R.A.J. Janssen, The energy of charge-transfer states in electron donor-acceptor blends: insight into the energy losses in organic solar cells, Adv. Funct. Mater. 19 (2009) 1939–1948.

[45] S.M. Menke, N.A. Ran, G.C. Bazan, R.H. Friend, Understanding Energy Loss in Organic Solar Cells: Toward a New Efficiency Regime, Joule. 2 (2018) 25–35.

[46] Y. Wang, Y. Wang, L. Zhu, H. Liu, J. Fang, X. Guo, F. Liu, Z. Tang, M. Zhang, Y. Li, A novel wide-bandgap small molecule donor for high efficiency all-small-molecule organic solar cells with small non-radiative energy losses, Energy Environ. Sci. 13 (5) (2020) 1309–1317.

[47] J. Benduhn, K. Tvingstedt, F. Piersimoni, S. Ullbrich, Y. Fan, M. Tropiano, K. A. McGarry, O. Zeika, M.K. Riede, C.J. Douglas, S. Barlow, S.R. Marder, D. Neher, D. Spoltore, K. Vandewal, Intrinsic non-radiative voltage losses in fullerene-based organic solar cells, Nat. Energy. 2 (2017) 17053.

[48] K. Vandewal, J. Benduhn, V.C. Nikolis, How to determine optical gaps and voltage losses in organic photovoltaic materials, Sustain. Energy Fuels. 2 (3) (2018) 538–544.

[49] S. Liu, J. Yuan, W. Deng, M. Luo, Y. Xie, Q. Liang, Y. Zou, Z. He, H. Wu, Y. Cao, High-efficiency organic solar cells with low non-radiative recombination loss and low energetic disorder, Nat. Photon. 14 (5) (2020) 300–305.

[50] N. Zarrabi, O.J. Sandberg, S. Zeiske, W. Li, D.B. Riley, P. Meredith, A. Armin, Charge-generating mid-gap trap states define the thermodynamic limit of organic photovoltaic devices, Nat. Commun. 11 (2020) 5567.

[51] C. Kaiser, O.J. Sandberg, N. Zarrabi, W. Li, P. Meredith, A. Armin, A universal Urbach rule for disordered organic semiconductors, Nat. Commun. 12 (2021) 3988.

[52] W. Tress, M. Yavari, K. Domanski, P. Yadav, B. Niesen, J.P. Correa Baena, A. Hagfeldt, M. Graetzel, Interpretation and evolution of open-circuit voltage, recombination, ideality factor and subgap defect states during reversible light-soaking and irreversible degradation of perovskite solar cells, Energy Environ. Sci. 11 (1) (2018) 151–165.

[53] X. Xia, T. Lau, X. Guo, Y. Li, M. Qin, K. Liu, Z. Chen, X. Zhan, Y. Xiao, P. Chan, H. Liu, L. Xu, G. Cai, N. Li, H. Zhu, G. Li, Y. Zhu, T. Zhu, X. Zhan, X. Wang, X. Lu, Uncovering the out-of-plane nanomorphology of organic photovoltaic bulk heterojunction by GTSAXS, Nat. Commun. 12 (2021) 6226.

[54] D.H. Lee, D.H. Kim, T. Kim, D.C. Lee, S. Cho, T. Park, Solid-solvent hybrid additive for the simultaneous control of the macro- and micro-morphology in non-fullerene-based organic solar cells, Nano Energy. 93 (2022), 106878.

[55] C. Guo, D. Li, L. Wang, B. Du, Z. Liu, Z. Shen, P. Wang, X. Zhang, J. Cai, S. Cheng, C. Yu, H. Wang, D. Liu, C. Li, T. Wang, Cold-Aging and Solvent Vapor Mediated Aggregation Control toward 18% Efficiency Binary Organic Solar Cells, Adv. Energy Mater. 11 (2021) 2102000.

[56] R.A. Jagt, T.N. Huq, S.A. Hill, M. Thway, T. Liu, M. Napari, B. Roose, K. Gałkowski, W. Li, S.F. Lin, S.D. Stranks, J.L. MacManus-Driscoll, R.L.Z. Hoye, Rapid Vapor-Phase Deposition of High-Mobility p-Type Buffer Layers on Perovskite Photovoltaics for Efficient Semitransparent Devices, ACS Energy Lett. 5 (8) (2020) 2456–2465.

[57] G.Y. Yoo, N. Nurrosyid, SeungJe Lee, Y. Jeong, I. Yoon, C. Kim, W. Kim, S.-Y. Jang, Y.R. Do, Newly Developed Broadband Antireflective Nanostructures by Coating a Low-Index MgF2 Film onto a SiO2 Moth-Eye Nanopattern, ACS Appl. Mater. Interfaces. 12 (9) (2020) 10626–10636.